GEOPHYSICS, VOL. 81, NO. 6 (NOVEMBER-DECEMBER 2016); P. R485–R501, 21 FIGS.
10.1190/GEO2016-0131.1

Time-lapse inverse theory with applications

Musa Maharramov[1], Biondo L. Biondi[1], and Mark A. Meadows[2]

ABSTRACT

Compaction in the reservoir overburden can impact production facilities and lead to a significant risk of well-bore failures. Prevalent practices of time-lapse seismic processing of 4D data above compacting reservoirs rely on picking time displacements and converting them into estimated velocity changes and subsurface deformation. This approach relies on prior data equalization and requires a significant amount of manual interpretation and quality control. We have developed methods for automatic detection of production-induced subsurface velocity changes from seismic data. We have evaluated a time-lapse inversion technique based on a simultaneous regularized full-waveform inversion (FWI) of multiple surveys. In our approach, baseline and monitor surveys are inverted simultaneously with a model-difference regularization penalizing nonphysical differences in the inverted models that are due to survey or computational repeatability issues. The primary focus of our work was the inversion of long-wavelength "blocky" changes in the subsurface model, and this was achieved using a phase-only FWI with a total-variation model-difference regularization. However, we have developed a multiscale extension of our method for recovering long- and short-wavelength production effects. We have developed a theoretical foundation of our method and analyzed its sensitivity to a realistic 1%–2% velocity deformation. The method was applied in a study of overburden dilation above the Gulf of Mexico Genesis field and recovered blocky negative-velocity anomalies above compacting reservoirs.

INTRODUCTION

Changes in reservoir rock properties as a result of stress changes induced by production are an important mechanism producing time-lapse effects (Holt et al., 2005). Velocity dependence on the confining stress and pore (fluid) pressure does not lend itself to easy analytical treatment and often exhibits hysteresis (i.e., dependence on the stress path). For compacting reservoirs and overburdens undergoing dilation above compacting reservoirs, it is more convenient to relate velocity and traveltime changes to strain, i.e., deformation. Unlike the effects of fluid substitution that are accurately quantifiable using Gassmann's equation, the existing velocity-strain relations are empirical, such as the R-factor method (Hatchell and Bourne, 2005; Herwanger, 2008). In the absence of counteracting effects (such as gas coming out of the solution), acoustic and shear velocities, as well as rock density increase within a compacting reservoir, with an increasing effective stress and dropping pore pressure. The acoustic and S-wave velocities typically decrease in a reservoir under water injection, with a decreasing effective stress and increasing pore pressure (Zoback, 2010). In a dilating, or stretching, overburden, rock density, acoustic and shear velocities decrease. Changes in acoustic velocity due to compaction or dilation are assumed proportional to strain and typically peak at 1%–3% of the unperturbed velocity magnitude, reaching tens of meters per second.

Detectability of changes in the subsurface properties induced by production was predicted in the rock-physics literature, and a time-lapse seismic method for the detection of fluid-substitution effects in reservoir rocks was proposed by Nur (1982), leading to a systematic use of imaging attributes for predicting changes in the subsurface-fluid parameters (Lumley et al., 1994; Lumley, 1995; Gawith and Gutteridge, 1996; Watts et al., 1996). Integration with static and dynamic rock-physics models, fluid simulation (Al-Najjar et al., 1999; Yuh et al., 2000; Landrø, 2001; Trani et al., 2011), and well logs (Gouveia et al., 2004) was the next logical step in the evolution of time-lapse seismic inversion, helping to separate time-lapse effects of fluid substitution from changes in other reservoir properties such as temperature and pressure. Bayesian time-lapse inversion (Buland and Ouair, 2006) emerged as a viable alternative

Manuscript received by the Editor 11 March 2016; revised manuscript received 19 June 2016; published online 7 November 2016.
[1]Stanford University, Stanford, California, USA. E-mail: musa@sep.stanford.edu; biondo@sep.stanford.edu.
[2]Chevron Energy Technology Company, San Ramon, California, USA. E-mail: mmeadows@chevron.com.

to deterministic methods, providing an estimate of the changes in the elastic material properties along with uncertainty bounds. Integration with dynamic reservoir models allows extending the uncertainty analysis to estimates of dynamic reservoir property changes (Grana and Mukerji, 2014).

All these time-lapse seismic inversion techniques share one common feature of relying on time shifts and amplitude differences extracted directly from baseline and monitor surveys. Indeed, prevalent practices of time-lapse seismic processing rely on picking time displacements and changes in amplitudes between pre- or poststack gathers, migrated baseline and monitor images or image gathers, and converting them into impedance changes and subsurface deformation (Johnston, 2013). This approach requires a significant amount of survey crossequalization, manual interpretation, and quality control.

At seismic resolution, subsurface-velocity changes can be classified as either short-wavelength "spiky," mostly occurring on a reservoir level, or long-wavelength blocky that may occur in the reservoir and overburden. Difference of the migrated baseline and monitor images can, in principle, provide sufficient information to quantitatively resolve the effect of blocky velocity changes from apparent (nonphysical) reflector shifts, and at least qualitatively estimate spiky changes from a combination of shifts and reflectivity changes. This approach can be automated using, e.g., image-difference tomography (Maharramov and Albertin, 2007). However, successful application of image-difference techniques still requires a significant prior data equalization effort to prevent contamination of the image difference with the effects of survey nonrepeatability. The main objective of this work is to develop an automated method for recovering production-induced subsurface changes that can significantly reduce or in some cases even eliminate data crossequalization requirements. This work largely focuses on recovering long-wavelength, small-magnitude velocity changes that manifest themselves in small time shifts detectable in prestack gathers after survey crossequalization. In particular, our field-data application focuses on recovering long-wavelength effects of overburden dilation. However, we demonstrate a multiscale extension of the method for recovering blocky and spiky velocity changes.

A recently proposed approach that avoids extraction of time-lapse information directly from data or image difference is based on using the high-resolution power of full-waveform inversion (FWI) (Sirgue et al., 2010a) to reconstruct production-induced changes from wide-offset seismic acquisitions (Zheng et al., 2011; Asnaashari et al., 2012; Routh et al., 2012; Raknes et al., 2013; Maharramov and Biondi, 2014a; Yang et al., 2014). However, while potentially reducing the amount of manual interpretation, time-lapse FWI is still sensitive to repeatability issues (Asnaashari et al., 2012), with coherent and incoherent noise (different survey geometries, source parameters, and environmental factors) potentially masking important production-induced changes. A linearized joint-inversion technique for time-lapse imaging that is more robust to repeatability issues was previously proposed by Ayeni (2011). In this paper, we describe a joint time-lapse FWI (Maharramov and Biondi, 2014a) that addresses repeatability issues by jointly inverting multiple survey vintages with a model-difference regularization. This joint-inversion approach is extended to include edge-preserving total-variation (TV) model-difference regularization (Maharramov et al., 2015b). We demonstrate the new method on synthetic and field-data examples of reflection seismic data by recovering small-magnitude, long-wavelength, blocky velocity changes that are due to overburden dilation.

THEORY

We present a time-lapse inverse-scattering theory as a study of the effects that slowness perturbations have on acoustic-wave propagation, and the inversion of a slowness perturbation from scattered wavefields without accurate knowledge of the background (unperturbed) slowness. We discuss different asymptotic representations of wavefields scattered by short- and long-wavelength perturbations and describe implications for the choice of a numerical method for inverting the perturbations. A theoretical sensitivity analysis of inversion accuracy to errors in the background model is followed by the description of a solution algorithm. This algorithm forms a basis for the numerical methods described and used in this paper.

Our goal is to adapt FWI to inverting time-lapse model changes. How does our choice of the FWI objective function affect sensitivity of the inversion to production-induced velocity changes? To answer this question, let us first analyze the sensitivity of the forward scattering to slowness perturbations at various perturbation scales. If a production-induced slowness perturbation δs of the baseline slowness model s_0 is oscillatory and has a zero mean, then the amplitude change of the scattered wavefield to a first order depends on the magnitude of the perturbation. However, the phase change of the scattered wavefield to a first order is insensitive to such zero-mean perturbations. On the other hand, the phase change of the scattered wavefield to a first order depends on the integral of slowness perturbation; i.e., the phase change is a proxy for the traveltime change (Slaney et al., 1984). Appendix A provides an independent sensitivity analysis of the forward-scattered wavefield to slowness changes based on the Born (equation A-7) and the Rytov (equation A-16) series. The phase-only Rytov approximation is applicable when the slowness perturbations are sufficiently small, as in equation A-23, and slowly varying in space, but possibly spread over a finite domain. The Born approximation, on the other hand, works best for perturbations within small domains or scattered diffractors (compare with Slaney et al., 1984). Indeed, the Rytov approximation with a strictly imaginary phase is equivalent to transmission traveltime analysis: The phase change of the scattered wavefield in equation A-25 is proportional to the traveltime delay due to a slowness perturbation δs.

For blocky model changes affecting primarily traveltimes, such as those due to the effects of overburden dilation, a method that inverts a slowness perturbation from the observed phase change (time shift) may adequately resolve the perturbation without using amplitude information. For inverting such blocky model changes, especially in the absence of reliable amplitude information in the observed data, we propose to use a phase-only FWI:

$$\| \exp i \arg \mathbf{d}_m - \exp i \arg \mathbf{u}(\mathbf{m}_m) \|_2^2 \rightarrow \min, \qquad (1)$$

where arg stands for the complex argument, $\mathbf{d}_m$ and $\mathbf{u}$ are the single-frequency components of the observed and predicted data sets, and $\mathbf{m}_m$ is the "monitor" (postproduction or after subsurface changes occurred) slowness model. We seek a slowness perturbation

$$\delta s = \mathbf{m}_m - \mathbf{m}_b \qquad (2)$$

that minimizes the quadratic misfit of the observed and predicted normalized wavefields in expression 1. In equation 2, $\mathbf{m}_b$ is a known "baseline" (preproduction or before subsurface changes occurred) model.

The first iteration of the frequency-domain FWI with a phase-only misfit function is equivalent to the linear phase-only Rytov inverse-scattering approximation of model updates. Subsequent iterations take into account the nonlinearity of the phase as a function of slowness. The optimization problem 1 is solved in the frequency domain.

If the amplitude information in the observed wavefield measurements is accurate, and if our wave propagation is dynamically accurate (i.e., produces accurate amplitudes), then we can use "phase-and-amplitude" frequency-domain FWI

$$\|\mathbf{d}_m - \mathbf{u}(\mathbf{m}_m)\|_2^2 \rightarrow \min, \tag{3}$$

where minimization is with respect to the monitor model $\mathbf{m}_m$. A slowness perturbation in equation 2 is nonzero only in the areas affected by production. Other a priori information may be available about δs, such as its "spikiness" (e.g., changes within fine layers) and "blockiness" (e.g., changes in "thick" layers, or stretching of the overburden). We can combine the objective functions 1 and 3 with a regularization or penalty term that promotes desirable features and penalizes undesirable ones:

$$\|\exp i \arg \mathbf{d}_m - \exp i \arg \mathbf{u}(\mathbf{m}_m)\|_2^2 + p(\mathbf{m}_m - \mathbf{m}_b) \rightarrow \min, \tag{4}$$

and

$$\|\mathbf{d}_m - \mathbf{u}(\mathbf{m}_m)\|_2^2 + p(\mathbf{m}_m - \mathbf{m}_b) \rightarrow \min, \tag{5}$$

where p is some penalty function of δs.

The phase-only inversion problems 1 and 4 have the advantage of not using the potentially unreliable dynamic wavefield information. Another significant advantage of the phase-only inversion is that in time-lapse problems of inverting long-wavelength small-magnitude model perturbations, Rytov inverse scattering and phase-only FWI are less sensitive to errors in the background model. For significant phase changes, phase wraps around the wavelength when exceeding it. Fitting peaks and troughs of the modeled and observed scattered wavefields (ignoring the amplitude information) then results in an ambiguity of the total phase change: The phase change can be resolved only within an integer multiple of the incident wavelength. This results in the well-known phenomenon of cycle skipping in FWI: Unless the FWI starting slowness model is accurate within the wavelength of the incident wave, the model cannot be resolved from signal phase information alone.

However, for time-lapse problems, the phase change due to a compact velocity anomaly of a sufficiently small magnitude is only a fraction of the wavelength. Indeed, after translating to the time domain, time shifts due to dilation in overburden peak at approximately 10 ms (Rickett et al., 2006; Maharramov et al., 2015a), i.e., about a third of the period for a 30 Hz signal. Therefore, phase changes (equivalently, time delays) of the scattered wavefields for small-magnitude long-wavelength perturbations that are of interest for us can still be translated into slowness changes using phase-change to traveltime conversion in expression A-25, if there is sufficient illumination of the anomaly. Moreover, those slowness changes are accurate to a first order regardless of errors in the background slowness. However, errors in the background velocity model will result in errors in the estimated velocity perturbation. For a slowness s and the corresponding velocity model v, we have

$$\delta s = \delta\left(\frac{1}{v}\right) \approx -\frac{\delta v}{v^2}. \tag{6}$$

If v_R and v_W are the right and wrong velocity models and δs is a slowness perturbation estimated using phase fitting, then

$$\delta v_W = -\delta s v_W^2 = -\delta s v_R^2 \left(\frac{v_W}{v_R}\right)^2 = \delta v_R \left(\frac{v_W}{v_R}\right)^2, \tag{7}$$

where δv_R and δv_W are the velocity perturbations estimated for the correct and wrong background velocity models, respectively. Equation 7 means that even with a wrong background velocity, qualitative information on the magnitude of velocity perturbation can still be extracted from the scattered wavefield. Note that location of the perturbation is determined by the illumination pattern of incident wavefields. Poor target illumination results in the ambiguity of the characteristic dimension L of the anomaly versus the perturbation magnitude δs as the two enter into expression A-25 for the phase change as a product. For example, lack of reflectors above the velocity anomaly results in an ambiguous vertical extent of the anomaly.

Note that our reliance on expression A-25 for the phase change requires transmission of the incident wave through the anomaly. For reflection seismic data, this implies that the baseline model in objective function 1 contains a model contrast at an approximately correct position of actual reflectors below and above the perturbation zone. In the presence of a diving-wave (refracted) signal, this requirement is not necessary.

Phase-only FWI problem 1 may produce a qualitatively accurate estimate of blocky, nonoscillatory production-induced model changes even when starting from a wrong baseline model. However, if using reflection seismic data, the baseline model should have model contrasts to generate synthetic reflections around the anomaly.

JOINT TIME-LAPSE FWI

To enhance the robustness of model-difference inversion and reduce nonrepeatability artifacts, we propose to invert for the baseline and monitor models simultaneously by solving either one of the following two optimization problems:

$$\alpha\|\mathbf{\Phi u}_b - \mathbf{\Phi d}_b\|_2^2 + \beta\|\mathbf{\Phi u}_m - \mathbf{\Phi d}_m\|_2^2 + \tag{8}$$

$$\delta\|\mathbf{WR}(\mathbf{m}_m - \mathbf{m}_b - \Delta\mathbf{m}^{\text{PRIOR}})\|_2^2 \rightarrow \min, \tag{9}$$

or

$$\alpha\|\mathbf{\Phi u}_b - \mathbf{\Phi d}_b\|_2^2 + \beta\|\mathbf{\Phi u}_m - \mathbf{\Phi d}_m\|_2^2 + \tag{10}$$

$$\delta\|\mathbf{WR}(\mathbf{m}_m - \mathbf{m}_b - \Delta\mathbf{m}^{\text{PRIOR}})\|_1 \rightarrow \min, \tag{11}$$

with respect to the baseline and monitor models $\mathbf{m}_b$ and $\mathbf{m}_m$. Problem 8,9 describes a time-lapse FWI with an L_2-regularization of the model difference in expression 9 (Maharramov and Biondi, 2014a). The second formulation 10,11 involves an L_1-regularization of the model difference (Maharramov et al., 2015b). Expression 10 corresponds to separate baseline and monitor misfits, and the term

11 represents regularization of the model difference. For a phase-only inversion, operator $\mathbf{\Phi}$ in the misfit terms 8 and 10 extracts amplitude-normalized wavefields from the observed and predicted data in the frequency domain, $\mathbf{\Phi} = \exp i \arg$, and it is equal to the identity map for a phase-and-amplitude inversion. In expressions 9 and 11, $\mathbf{R}$ and $\mathbf{W}$ denote the regularization and weighting operators, respectively. If $\mathbf{R}$ is the gradient magnitude operator

$$\mathbf{R}f(x_1, x_2, x_3) = \sqrt{f_{x_1}^2 + f_{x_2}^2 + f_{x_3}^2}, \tag{12}$$

then expression 11 becomes the TV seminorm. The latter case is of particular interest in this work as the minimization of the L_1-norm of gradient may promote blockiness of the model difference, potentially reducing oscillatory artifacts (Rudin et al., 1992; Aster et al., 2011).

A joint-inversion approach has been applied earlier to the linearized-waveform inversion (Ayeni and Biondi, 2012). In Maharramov and Biondi (2014a), simultaneous FWI problem 8,9 was studied with an L_2 model-difference regularization term 9. In Maharramov et al. (2015a, 2015b), simultaneous FWI problem 10,11 was studied with a model-difference TV-regularization term 11.

The model-difference regularization weights $\mathbf{W}$ and, optionally, the prior $\Delta\mathbf{m}^{\text{PRIOR}}$ may be obtained from prior geomechanical information. For example, a rough estimate of production-induced velocity changes can be obtained from time shifts (Barkved and Kristiansen, 2005; Hatchell and Bourne, 2005) and used to map subsurface regions of expected production-induced perturbation and optionally provide a difference prior. However, successfully solving the L_1-regularized problem 10,11 is less sensitive to the choice of a weighting operator $\mathbf{W}$. For example, we show below that the TV regularization using operator 12 with $\mathbf{W} = 1$ recovers nonoscillatory components of the model difference, whereas the L_2 approach would result in either smoothing or uniform reduction of the model difference. Optimization problem 8,9 is a large-scale nonlinear least-squares minimization problem with Tikhonov regularization (Tikhonov and Arsenin, 1977; Aster et al., 2011) that can be solved using, for example, nonlinear conjugate gradients (Nocedal and Wright, 2006). However, problem 10,11 has a nondifferentiable objective function and can be computationally challenging. We get around the nondifferentiability by smoothing the regularization operator 12 near the zero gradient

$$\mathbf{R}f(x_1, x_2, x_3) = \sqrt{f_{x_1}^2 + f_{x_2}^2 + f_{x_3}^2 + \epsilon^2}, \tag{13}$$

where $\epsilon = 10^{-5}$ was experimentally found to produce the best results in our experiments, with operator 13 applied to the slowness difference. Optimization solver is implemented in double precision to handle potentially large gradient oscillations of the resulting objective function. However, single-precision arithmetic is adequate for gradient computation of the data-misfit terms in equation 10. The localized nature of time-lapse changes and good estimates of lower bounds for slowness differences allow the relatively simple smoothing approach of equation 13 to be quite successful in practice. However, application of TV-regularized inversion to non-4D problems, where the inverted model is not localized and model contrasts may widely range in amplitude, may require a more sophisticated solution approach for minimizing the nonsmooth objective function 10,11 directly, such as, for example, the alternating direction method of multipliers (Goldstein and Osher, 2009; Boyd et al., 2011). Another important aspect of solving the regularized optimization problem 10,11 is the selection of a regularization parameter δ. In our tests, we start from an initial value of δ used in earlier similar inversion experiments. As we progress through the iterations of conjugate gradients, we inspect the updates to the objective function and objective-function gradient from the data-misfit terms in equation 10 and the corresponding model-difference regularization term in equation 11. If contributions from the misfit terms dominate the update while the model difference is still contaminated with oscillatory artifacts, we increase the value of δ. On the other hand, if the algorithm stops fitting the data at very early iterations, we reduce δ. In our experiments, this procedure produces a suitable value for δ within a few initial iterations of conjugate gradients. This regularization parameter is then reused for the remainder of iterations. Interestingly, in our frequency-domain inversion experiments for synthetic and field data, a single value of δ can be reused for frequency ranges of up to 10 Hz, significantly reducing parameter fine-tuning overhead. However, this obviously depends on the frequency content of the data.

APPLICATION TO REFLECTION DATA

In our earlier work (Maharramov et al., 2015b), we successfully applied the simultaneous time-lapse FWI method 10,11 to noisy synthetic data and demonstrated a stable recovery of a blocky model difference in the presence of variable repeatability issues. The repeatability issues simulated in that work included different source and receiver numbers, locations and depths, different source signatures, and very noisy 7 dB signal-to-noise ratio acquisitions. Inclusion of the TV regularization term 11 successfully reduced oscillatory artifacts and preserved the blocky nature of the true model difference. However, that experiment involved phase-and-amplitude FWI using reflection and refraction data, making the inversion very well-constrained and using the full high-resolution power of FWI. Many important examples of time-lapse applications indeed involve similar inversion targets, and it was originally expected that applications like that would be the primary target of the developed joint time-lapse FWI technique.

However, the field time-lapse data obtained by Stanford Exploration Project for applying and testing our method forced us to change the original plan. Survey and target parameters of the field data precluded use of diving waves. Uncertainty in the starting model meant that sensitivity to inaccurate starting models and cycle skipping could be an issue. It was at this time that we developed the time-lapse inverse theory, aiming to adapt our inversion technique to the challenging data set in hand. The theory demonstrated a sensitivity of phase-only inversion to small-magnitude blocky velocity changes in the overburden that were of particular interest for the field data in question (see expression A-25). Qualitative accuracy of the inversion for wrong FWI starting models was established as well (see equation 7). The purpose of the following three sections is to provide numerical corroboration of the theoretical analysis of the prior sections, and lay the groundwork for an application to field data.

SYNTHETIC MODEL

In our earlier work (Maharramov et al., 2015b), we demonstrate the effective recovery of blocky velocity anomalies from long-offset acquisitions in the presence of noise and repeatability issues. Here,

we demonstrate the recovery of blocky anomalies in the more challenging case of phase-only inversion of reflection-only synthetic data. Conceptually, our synthetic example is similar to the field data studied by Maharramov et al. (2015a).

As a baseline model, we use the flat reflector model of Figure 1. The target reflector (reservoir) is located at a depth of 3900 m, and the monitor (perturbed) model has two velocity anomalies — a positive +300 m/s change due to compaction and fluid substitution within the reservoir and a blocky negative velocity change in the overburden above the reservoir, peaking at −50 m/s (see Figure 2). No physical reflector movement is prescribed.

For generating synthetic data, we used towed-streamer acquisition geometry with a maximum offset of 5 km common to the baseline and monitor because this experiment focused on demonstrating the sensitivity of our method to subsurface changes when the phase-only FWI objective function and reflection-only data are used. Note that the relatively small maximum offset to target depth ratio for the model of Figure 1 means the target is illuminated only by reflected energy. Figure 3 shows common-midpoint gathers above the center of the target reservoir for the baseline (blue) and monitor (red) surveys. Signals that travel vertically through the anomaly are delayed the most, whereas longer offset reflections are delayed less because they largely bypass the anomaly. Reflections above the anomaly show no time shift.

Figure 3 represents a typical overburden dilation effect on arrival times: Timeshifts accumulate with distance traveled through the low-velocity anomaly, peaking at small but tangible delays to the order approximately 10 ms near the reservoir top (Hatchell and Bourne, 2005; Johnston, 2013).

TIME-LAPSE INVERSION FROM REFLECTION DATA

The results of parallel difference and crossupdating (Maharramov and Biondi, 2014a) are shown in Figures 4 and 5. Note that neither method succeeds in recovering the blocky anomaly. The FWI starting model used in these experiments was produced by smoothing the true baseline model using a 1920 m smoothing window. A frequency-domain 2D FWI (Sirgue et al., 2008, 2010b) was conducted using frequency continuation for 23 frequencies ranging from 3 to 30 Hz. A phase-only inversion was conducted using the objective function in equation 1 to ignore any amplitude information in the data. Frequency spacings were selected using the technique of Sirgue and Pratt (2004). Ten iterations of the conjugate gradients method were used per single frequency, with the model-difference TV regularization term smoothed as shown in equation 13.

The result of a phase-only simultaneous inversion with a TV model-difference regularization (equations 10,11) is shown in Figure 6. The result is qualitatively accurate although peak magnitudes are underestimated due to TV regularization, as discussed by Meyer (2001).

To recover the short-wavelength changes within the reservoir, we used a cascaded or "hierarchical" inversion approach (Tadmor et al., 2004; Maharramov and Biondi, 2014b) and supplied the result of Figure 6 as a model difference prior to inversion problem 8,9, with Tikhonov regularization of the model difference. Note that the resulting model shown in Figure 7 features long- and short-wavelength velocity perturbations. And again, the reservoir perturbation is underestimated due to the strong regularization. Note the leakage of a small-amplitude velocity anomaly below the reservoir. This is the result of a lack of strong reflectors below the reservoir (see Figure 3).

To assess effectiveness of the inversion, in Figure 8a and 8b, we show monitor images migrated using the true monitor and true baseline models, respectively. Note that the overestimated velocities in the overburden result in a downward reflector shift in Figure 8b. However, migrating the monitor data using the sum of the baseline model and the inverted blocky anomaly of Figure 6 results in the image of Figure 9a: The downward shift of reflectors in the overburden is now significantly reduced.

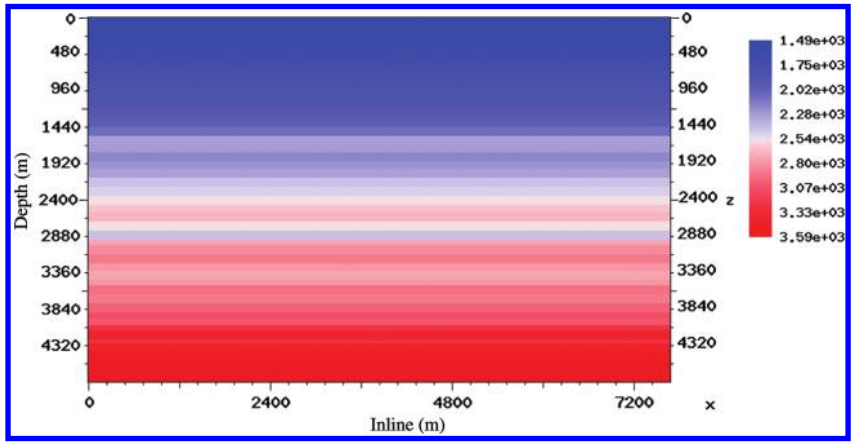

Figure 1. The true baseline model. A flat reflector model to study the sensitivity of FWI of short-offset reflection data to small velocity perturbation in the overburden.

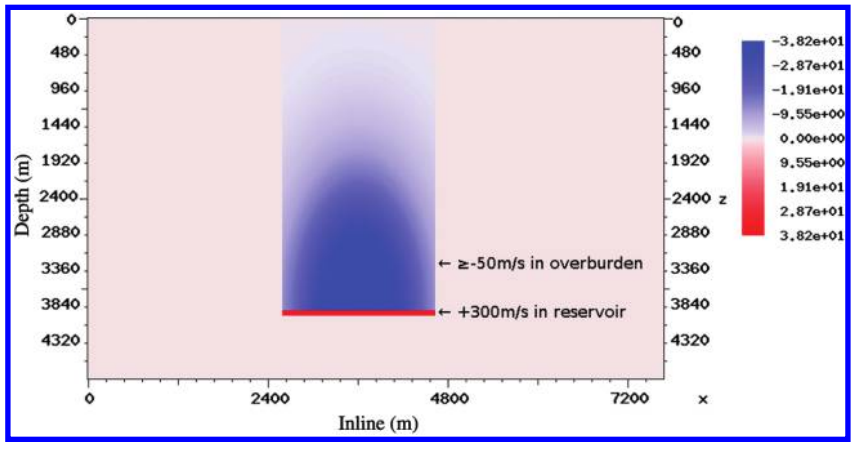

Figure 2. The true model difference is a combination of a positive +300 m/s velocity change in a target reflector at a depth of 3900 m, and a negative velocity change in the overburden above the reflector, peaking at −50 m/s. We investigate the sensitivity of simultaneous time-lapse FWI to small-magnitude blocky velocity changes in the overburden.

SENSITIVITY TO CYCLE SKIPPING

Time-lapse scattering theory predicts that a qualitatively accurate inversion of blocky anomalies from phase information can be achieved despite inaccurate FWI starting models (see equation 7). Here, we study the method's sensitivity to starting models and cycle skipping by inverting two isolated anomalies shown in Figure 10. We chose a more challenging test than the previous model of Figure 2 to make it more sensitive to the accuracy of our inversion: Inversion artifacts may not only distort each anomaly but also violate their separation.

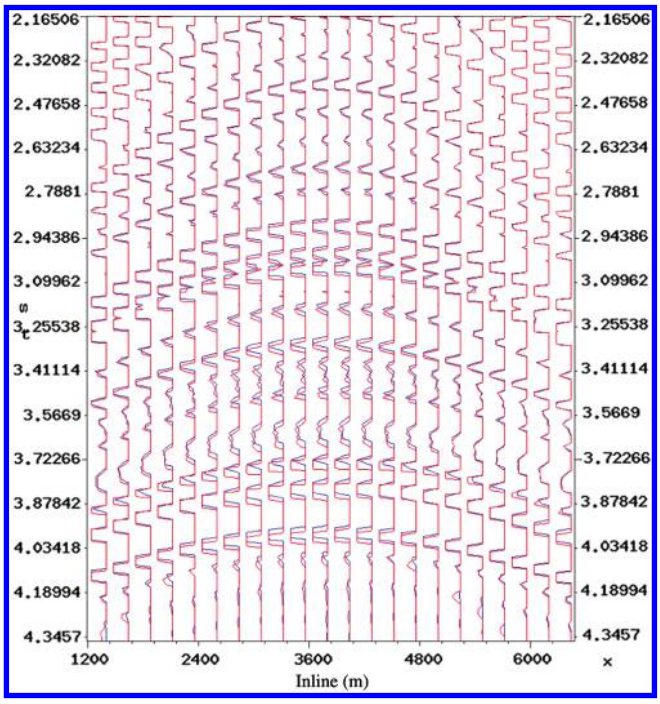

Figure 3. Time shifts observed in common-midpoint gathers centered above the target reservoir (blue is baseline and red is monitor). Traveltimes of the monitor near-offset reflections traveling through the negative velocity anomaly of Figure 2 are slightly delayed.

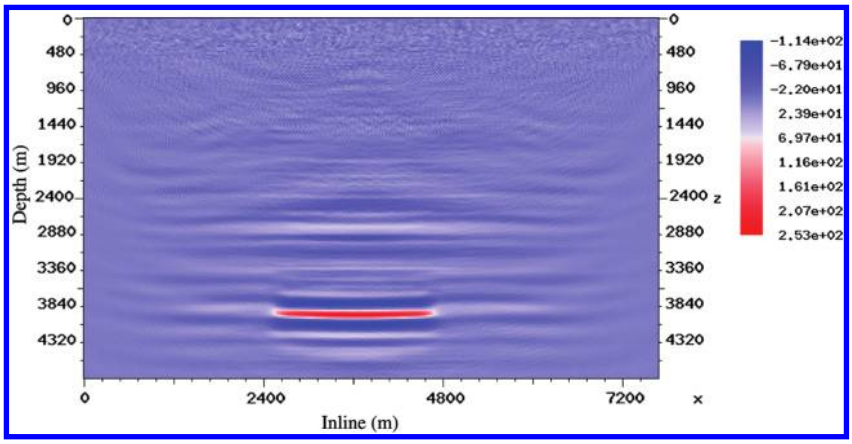

Figure 4. The parallel-difference method fails to resolve the long-wavelength velocity changes of Figure 2 and produces negative short-wavelength artifacts around the target reflector.

Figure 11 demonstrates the recovery of two separate overburden anomalies when the FWI starting velocity is a smoothed true baseline velocity produced using a 1920 m smoothing window. As before, the inversion is in good agreement with the true difference. Here, we invert only for the blocky component, ignoring the spiky component within the reservoir that is caused by fluid substitution and reservoir compaction.

The result of starting FWI from a wrong velocity (that contains a wrong high-wavenumber component) is shown in Figure 12. We deliberately used a weak regularization parameter for model-difference regularization to demonstrate the effect of diverging baseline and monitor models on the inverted model difference. Either one or both of the baseline and monitor inversions cycle skipped, and the models diverged from each other sufficiently far to contaminate the model difference with strong artifacts. The artifacts almost completely masked one of the anomalies and contaminated areas not affected by production with false positives.

Figure 13 shows the result of using a stronger TV regularization, as prescribed by our time-lapse inverse theory. By choosing a stronger model-difference regularization, we ensure a greater conformity between the two models, that the two models cycle skip "in synchrony." As a result, we are still able to qualitatively recover the anomalies, although with strongly underestimated velocities (compare with equation 7).

Note that the magnitude of the slowness change is underestimated as a result of the stronger model-difference regularization in expression 11. Adopting the recommendations of Meyer (2001) can alleviate this problem, so that slowness magnitudes can be inverted more accurately. However because of equation 7, the wrong velocity background would still result in a quantitatively wrong velocity perturbation. Traveltime delays can be translated into accurate slowness changes even for wrong backgrounds as shown in expression A-25 (so long as the reflected signal is present in predicted baseline and monitor data and traveltimes differ by less than $2\pi/\omega$), but a quantitatively accurate estimate of the velocity difference still requires knowledge of accurate background velocity.

Numerical experiments have borne out our theoretical predictions with regard to the sensitivity of phase-only time-lapse FWI of reflection data to realistic production-induced time shifts, and the method's stability with regard to inaccurate FWI starting models. In the following sections, we apply the method to field data for a reservoir in which production was associated with a significant overburden dilation and reflection traveltime changes.

GENESIS FIELD

The Genesis field, operated by Chevron, is located 241 km (150 mi) southwest of New Orleans in the Green Canyon area of the central Gulf of Mexico, in approximately 770–830 m of water (Magesan et al., 2005). Oil was found in several late Pliocene through early Pleistocene deepwater reservoirs. Most of the field's oil and gas reserves are in the early Pleistocene Neb 1, Neb 2, and Neb 3 reservoirs that are the primary subject of this study (see Figure 14).

First oil production began in January 1999. A 3D seismic survey was shot in 1990, and a time-lapse 3D survey was shot in October 2002 with

the aim of improving field management (Hudson et al., 2005; Magesan et al., 2005). Cumulative production from the field at the time of the monitor survey was more than 57 million barrels of oil (MMBO), 89 million cubic feet of gas (MMCFG), and 19 million barrels of water (MMBW) (Hudson et al., 2005).

In addition to fluid-substitution effects, producing reservoirs compact, thereby increasing the depth to the top of the reservoirs and causing overburden dilation (Johnston, 2013). A time-lapse study performed by Chevron (Hudson et al., 2005) indicated significant apparent kinematic differences in the Pleistocene reservoir interval. Time shifts were observed for the producing reservoirs and Illinoisan wet sands above Neb 1. Kinematic differences were attributed to a time shift caused by subsidence at the top of the uppermost reservoir, subsidence of the overburden, and overburden dilation (Hudson et al., 2005).

Processing parameters for the baseline and monitor surveys and the subsequent time-lapse processing by Chevron are described by Magesan et al. (2005). The baseline survey had a maximum offset of 5 km, and the monitor survey had a maximum offset of 7.3 km. Both surveys used a bin size of 12.5×37 m. For the purpose of time-lapse analysis, the acquired data had been subjected to preprocessing and imaging steps that included data equalization, spherical divergence correction, source and receiver statics, global phase rotation, time shift, amplitude scaling, global spectral matching, and crossequalization (Magesan et al., 2005).

These preprocessed data were used by Chevron in Kirchhoff time migration of the baseline and monitor surveys to produce 3D images. A single inline section of the baseline image is shown in Figure 15. The corresponding monitor and baseline image difference is shown in Figure 16. As noted by Hudson et al. (2005), the image difference is contributed to by time shifts at the Illinoisan sands (upper event) and Neb 1 (lower event) in Figure 16 (compare with Figure 1 of Hudson et al., 2005).

2D INVERSION

The purpose of this experiment was to see whether joint regularized time-lapse FWI could resolve some of the production-induced model differences, thus providing additional insight into reservoir depletion patterns and optimal infill drilling strategies. As our first processing step, we performed separate baseline and monitor 2D FWI of a single inline section. We extracted a single north–south inline section corresponding to the image in Figure 15 from both surveys and sorted them into shot gathers with a mini-

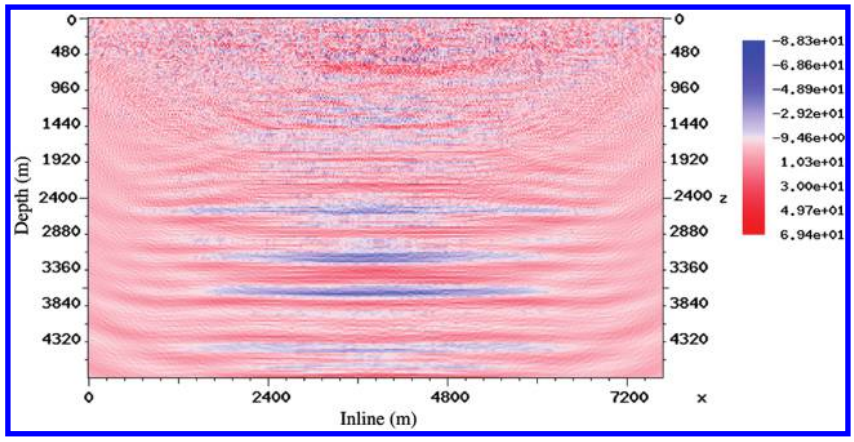

Figure 5. The crossupdated FWI method crossequalizes the baseline and monitor models but still fails to resolve the long-wavelength overburden changes of Figure 2.

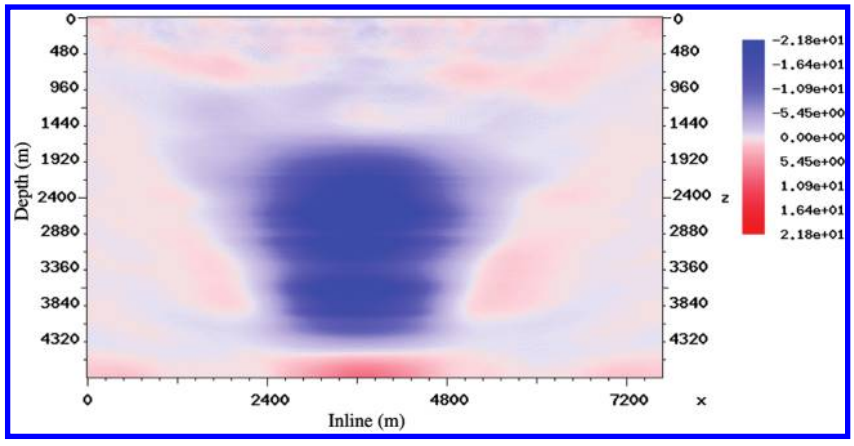

Figure 6. Simultaneous FWI with a TV model-difference regularization resolves the long-wavelength overburden changes of Figure 2, but underestimates the maximum change, depending on the regularization strength.

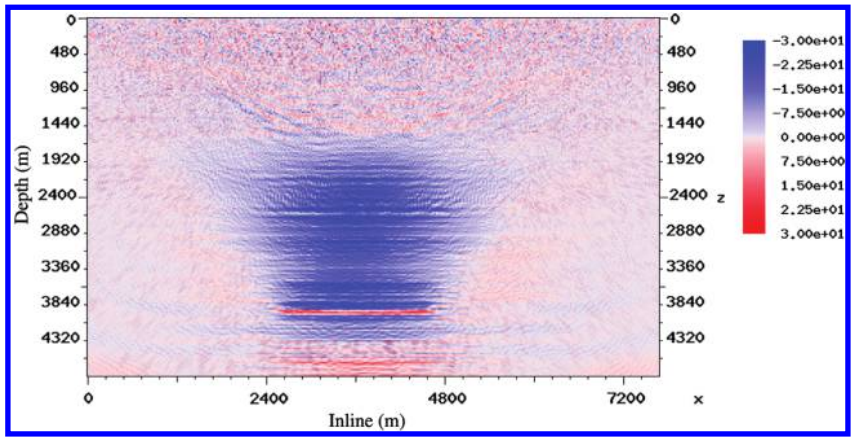

Figure 7. Simultaneous FWI using Tikhonov model-difference regularization with the long-wavelength inversion of Figure 6 supplied as a prior. Note that such a multiscale approach can now resolve the short-wavelength positive-velocity changes of Figure 2. Strong Tikhonov regularization results in underestimated velocity changes within the reservoir, but correctly locates the anomalies.

mum offset of 350 m and a maximum offset of 4700 m. This provided 1264 shots per survey with up to 175 receivers per shot. A frequency-domain 2D FWI (Sirgue et al., 2008, 2010b) was conducted over the frequency range of 3–30.7 Hz. Frequency spacings were selected using the technique of Sirgue and Pratt (2004). As noted above, the data provided to Stanford Exploration Project had undergone amplitude preprocessing that included a spherical divergence correction. Furthermore, accurate handling of the amplitudes in 2D FWI of 3D field data requires a 3D-to-2D data transformation (Auer et al., 2013). Because the data exhibited significant time shifts at the reservoir level (Hudson et al., 2005) that can be readily observed even at large offsets (see Figure 17), we decided to use a "phase-only" inversion and ignored amplitude information in the data (Fichtner, 2011).

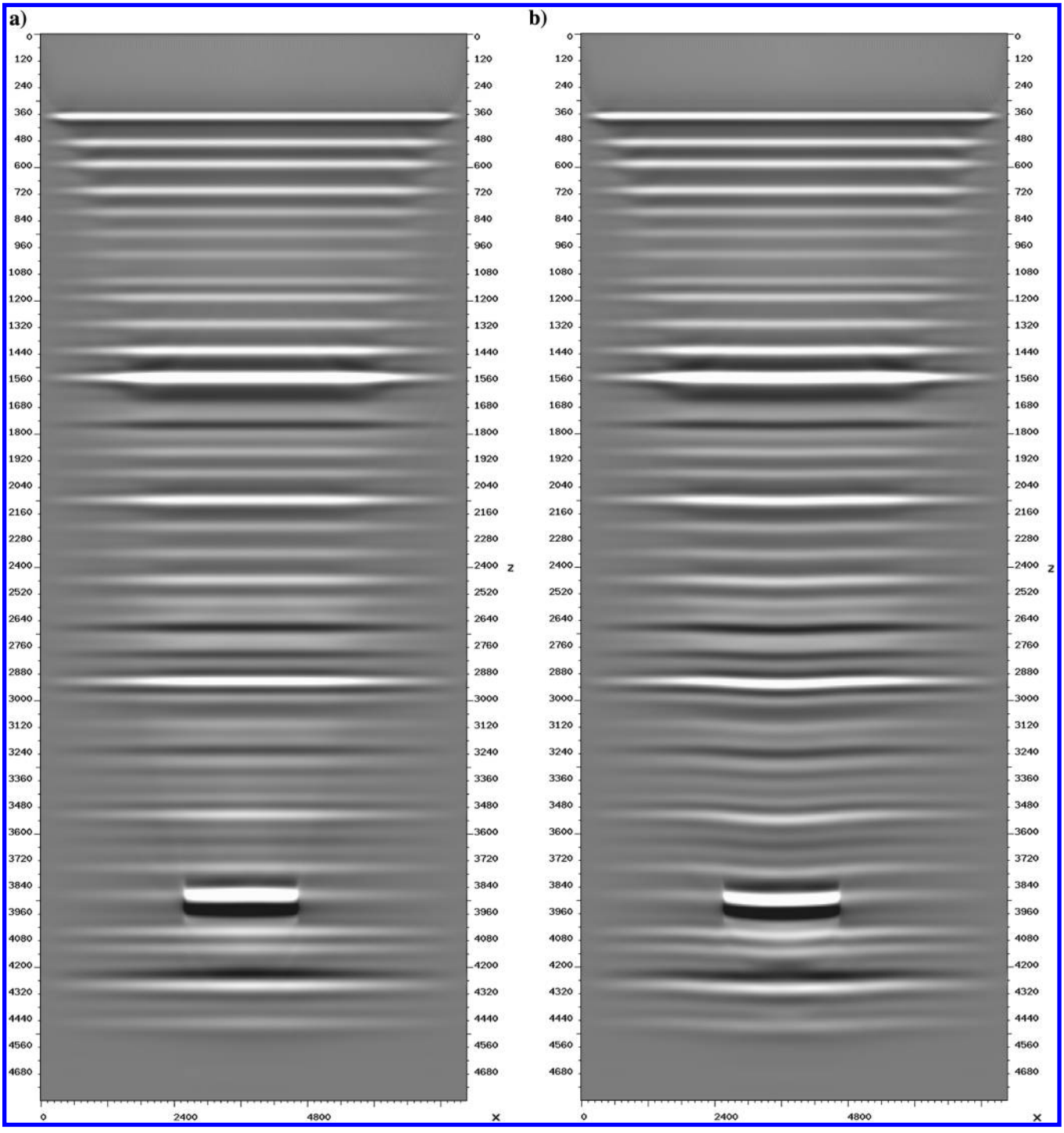

Figure 8. (a) True monitor image. (b) Monitor migrated using the baseline velocity model. Note that overestimated velocity in the overburden results in a downward reflector shift in the right image.

The result of baseline inversion is shown in Figure 18. To build a starting model for the FWI, we converted Chevron's rms time-migration velocity model to an interval velocity using the Dix equation, and smoothed the result using a triangular filter with a 41-sample window. Observe that FWI succeeded in resolving fine features, and oriented them consistently along the dip structure of the time-migrated image in Figure 15. Close-up views of the model area covering the Illinoisan sands and the reservoirs are shown in Figure 19a and 19c.

The result of parallel differencing is shown in Figure 20a. Although significant model changes appear to be concentrated around the target area, this result is not interpretable, either qualitatively or quantitatively because it is contaminated with oscillatory artifacts and it overestimates the magnitudes of velocity

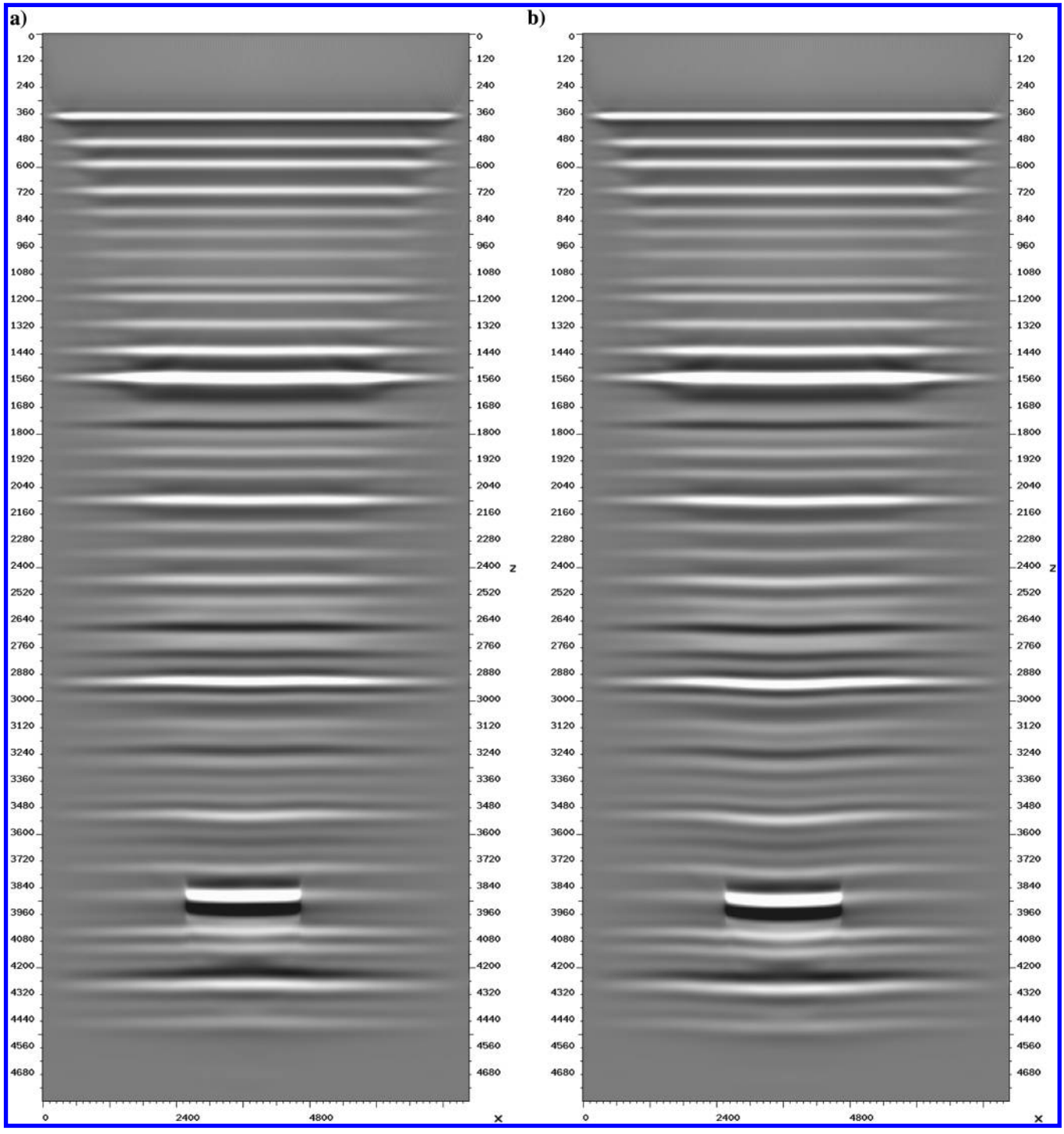

Figure 9. (a) Monitor image migrated using the sum of the baseline model and inverted model difference of Figure 6. (b) Monitor migrated using the baseline velocity model. Note that reflector shift in the overburden has been significantly reduced in the left image.

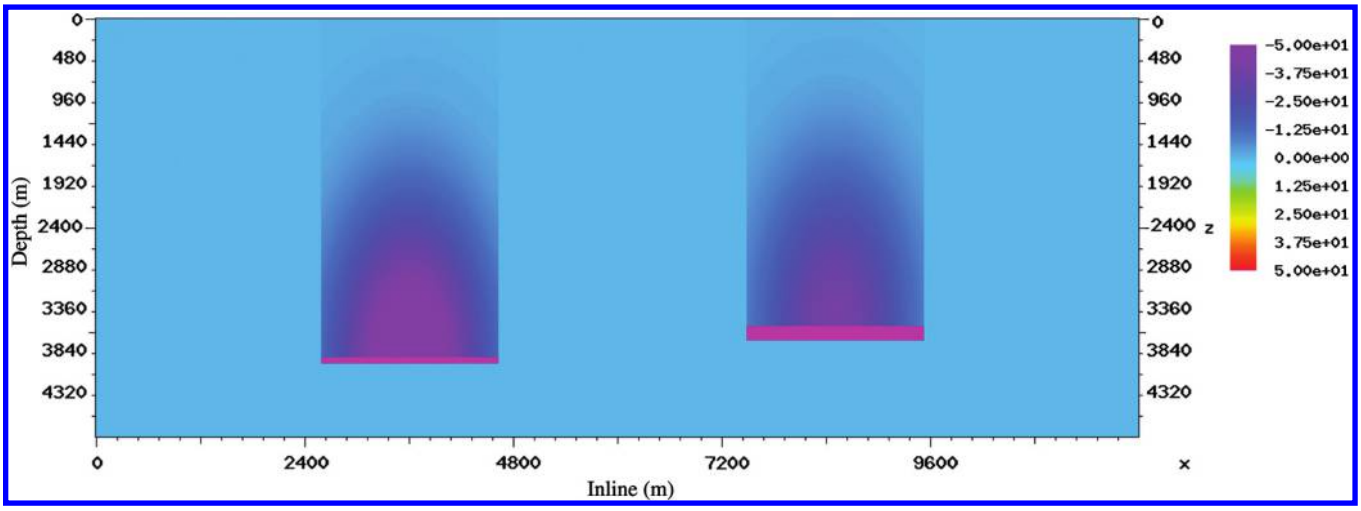

Figure 10. True model difference for demonstrating the inversion of multiple overburden anomalies.

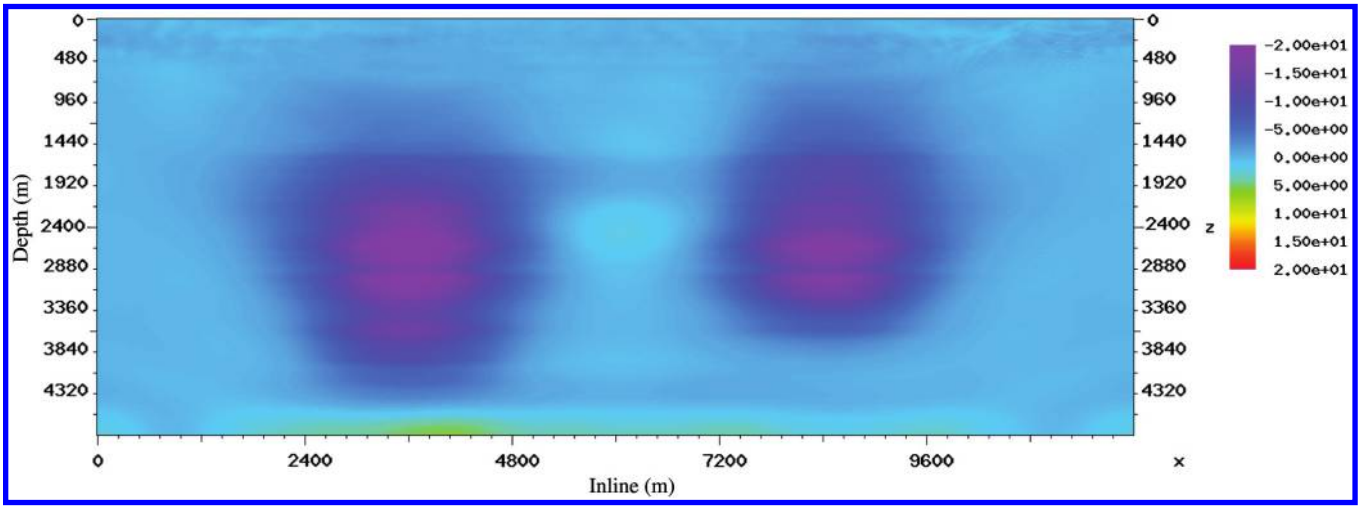

Figure 11. Inversion of the two long-wavelength overburden anomalies of Figure 10 using simultaneous time-lapse FWI with a TV model-difference regularization.

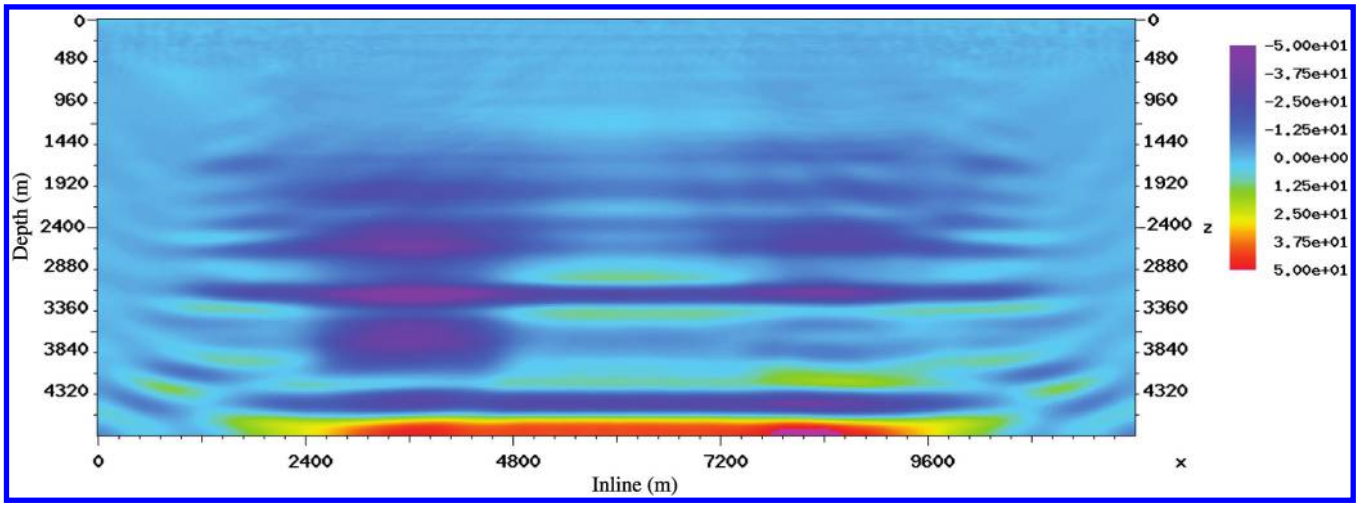

Figure 12. Inversion of the two long-wavelength overburden anomalies of Figure 10 starting from a wrong initial model and using weak regularization (a small regularization parameter). FWI cycle skipped, and the baseline and monitor inversions diverged, contaminating the difference with cycle-skipping artifacts.

perturbations. This result is consistent with our earlier assessment of conventional time-lapse FWI techniques tested on synthetic data (see Maharramov and Biondi, 2014a; Maharramov et al., 2015b).

Then, we conducted the simultaneous, TV-regularized time-lapse FWI formulation 10,11. We set $\alpha = \beta = 1$ and carried out multiple experiments with the value of the regularization parameter δ ranging from $\delta = 100$ to 1000. The weighting operator $\mathbf{W}$ was set to one inside the larger target area shown in Figure 19a and tapered off to zero outside.

The results of inverting the model difference for $\delta = 100$, 500, and 1000 are shown in Figure 20b, 20c, and 20d, respectively. Gradual increase of the regularization parameter results in the removal of most model differences with the exception of a negative velocity perturbation in the overburden, peaking at approximately 3.6 and 3.9 km depth (see Figure 19b and 19d). Such perturbations are consistent with overburden dilation due to the compaction of stacked reservoirs, with more significant dilation in the wet Illinoisan sands than the surrounding shales (Rickett et al., 2007). The zone of negative velocity change appears to extend upward into the overburden in a direction roughly orthogonal to the reservoir dip (see Figure 20d). Two negative velocity changes at approximately 10 and 11.5 km inline persist with increasing regularization, and may represent dilation effects associated with the production from deeper reservoir (compare with Figure 3 of Rickett et al., 2007).

Figure 21 plots the inverted velocity change against difference of the migrated monitor and baseline images produced using reverse time migration. Migration was conducted using the same (starting FWI) velocity for baseline and monitor. The image difference is strongest at a 3.6 km depth, corresponding to the Illinoisan sands, and approximately 3.9 km — the overburden above Neb 1.

The estimated maximum negative velocity change of −45 m/s above the stacked reservoirs is consistent with the earlier estimates of time strain in the overburden (Rickett et al., 2007). Indeed, local time strain, physical strain, and partial velocity change are related by the equation (Hatchell and Bourne, 2005)

$$\frac{d\tau}{dt} \approx \frac{\Delta t}{t} = \frac{\Delta z}{z} - \frac{\Delta v}{v}, \tag{14}$$

where τ, t, z, and v denote the observed time shift, vertical traveltime, depth, and velocity, respectively.

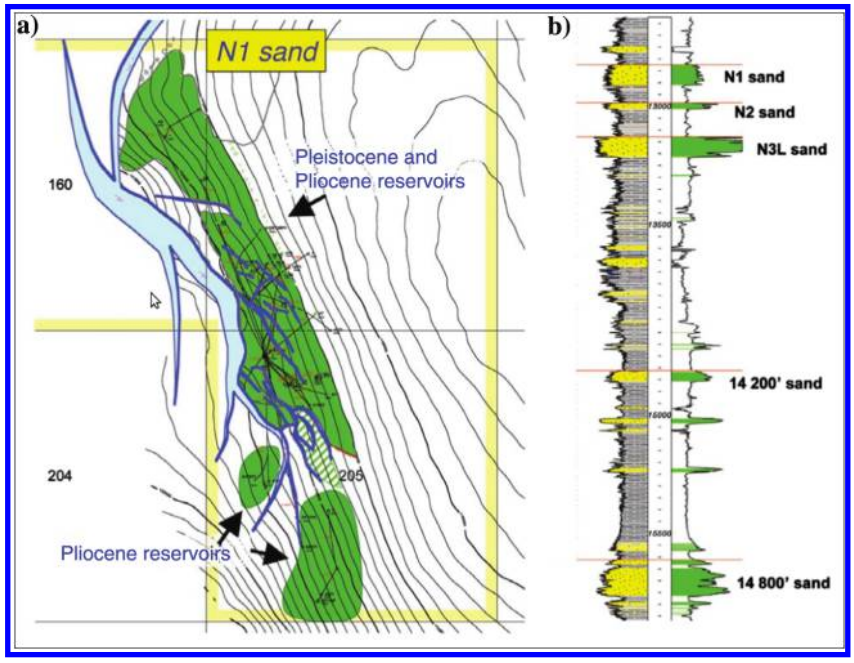

Figure 14. The Genesis field (from Magesan et al., 2005).

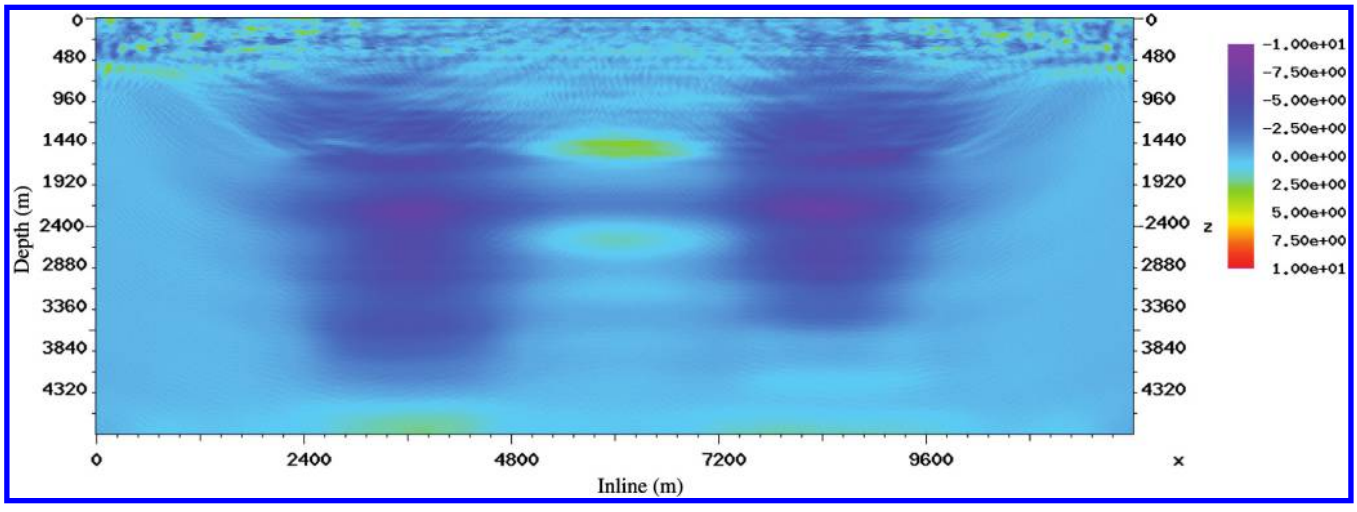

Figure 13. Inversion of the two long-wavelength overburden anomalies of Figure 10 starting from the same bad initial model, but using a stronger regularization (a larger regularization parameter). FWI still cycle skipped; however, the strong model-difference regularization kept the baseline and monitor within the characteristic wavelength of the overburden anomalies. The resulting model-difference inversion is qualitatively accurate (compare with Figure 11), albeit the stronger regularization has resulted in underestimated velocity magnitudes.

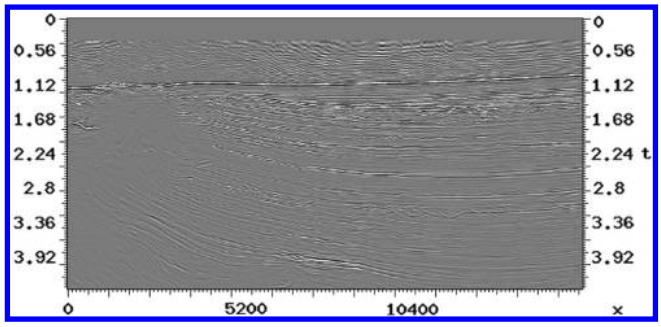

Figure 15. A north–south inline section of the baseline Genesis image produced by Chevron (vertical axis two-way traveltime in seconds and horizontal axis inline in meters).

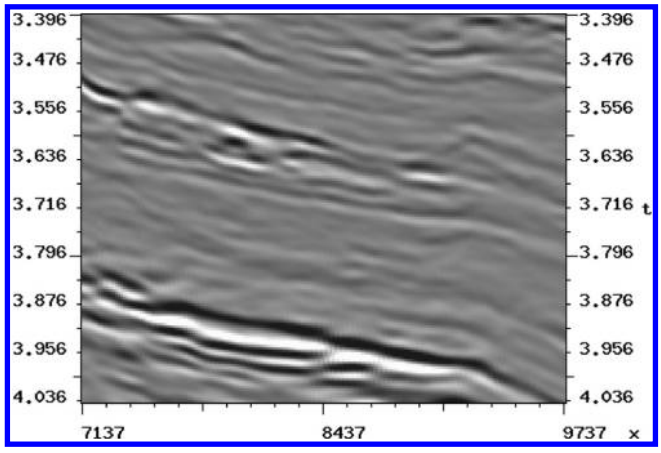

Figure 16. Monitor and baseline image difference obtained from the 3D time-migration images provided by Chevron, which corresponds to the inline section of Figure 15. Production-induced changes stand out at approximately 3.5 s (wet Illinoisan sands) and 4 s two-way traveltimes — stacked Neb 1, 2, and 3 reservoirs.

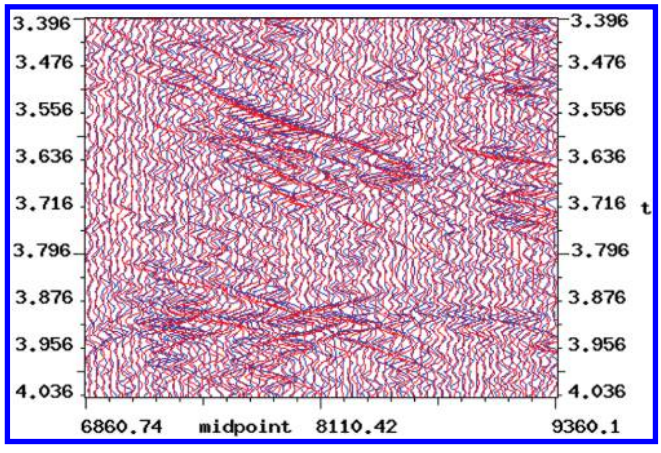

Figure 17. Production-induced changes resulted in measurable time shifts between the surveys. Shown here are the time shifts between the baseline (blue) and monitor (red) common-offset gathers, 1074 m offset.

Assuming, following Hatchell and Bourne (2005), that

$$\frac{\Delta v}{v} = -R\frac{\Delta z}{z}, \tag{15}$$

where the factor R is estimated to be 6 ± 2 for the Genesis overburden (Hodgson et al., 2007), we obtain

$$\frac{\Delta v}{v} = -\frac{R}{R+1}\frac{\Delta t}{t} \approx -\frac{\Delta t}{t} \approx -\frac{d\tau}{dt}. \tag{16}$$

Maximum time strains in the Genesis overburden are estimated to be approximately $+2\%$ (Rickett et al., 2007), yielding the maximum negative velocity change of

$$\Delta v \approx -0.02 \times 2800 \text{ m/s} = -56 \text{ m/s}, \tag{17}$$

where the estimated P-wave velocity of 2800 m/s at a 3.6 km depth was taken from the output of FWI.

DISCUSSION AND PERSPECTIVES

In this work, we provided a theoretical justification for the time-lapse inversion methods of Maharramov et al. (2015a, 2015b) and demonstrated recovery of short- and long-wavelength velocity anomalies from narrow-offset reflection seismic data. We envisage widespread application of the simultaneous FWI with model-difference regularization and hierarchical multiscale inversion in applications ranging from applied geophysics to electromagnetic and optical scattering.

Simultaneous time-lapse FWI with a TV difference regularization can achieve a robust estimation of velocity changes in the overburden that are induced by reservoir compaction and overburden dilation. The method preserves the blocky nature of model difference while penalizing unwanted oscillations. As a model-space technique, the simultaneous 4D FWI does not require prior cross-equalization between baseline and monitor data sets. The model-difference regularization penalizes differences in the inverted models that are due to nonrepeatable acquisition or numerical inversion errors. For example, where the monitor model is poorly constrained due to a facility gap in the monitor survey, the model-difference regularization causes the models to more closely match, implicitly using information in the baseline survey to invert the monitor model. Spurious oscillatory model-difference artifacts resulting from a slight misalignment of velocity contrasts between the inverted models (see Figures 5 and 20a) can be easily removed using a TV-based regularization, whereas nonoscillatory long-wavelength changes are retained. In the context of a cascaded or hierarchical inversion, once long-wavelength model changes have been extracted, alternative L_1-based regularization techniques (see, e.g., Ma et al., 2015) can be subsequently applied in the inversion of short-wavelength model changes. Obviating explicit requirements for survey crossequalization may lead to a less labor-intensive and more automated 4D analysis, as survey data can be supplied to the simultaneous FWI algorithm following surface-related multiple suppression, bypassing conventional 4D processing. However, 4D FWI may be applied to crossequalized surveys as well, and used after, or in parallel with, the conventional 4D processing for purposes of validation or accuracy improvement.

Application of the method to large-scale 3D time-lapse problems generally requires major computational resources. Indeed, in our experiments, separate monitor and baseline FWIs were followed by two more crossupdating inversions, and solution of the simultaneous FWI problem 8,9 or 10,11. The latter is roughly equivalent to the cost of two FWIs; hence, the total cost may reach six times the computational cost of a single FWI.

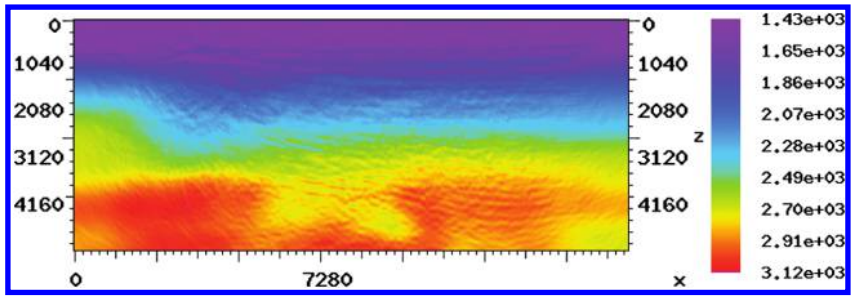

Figure 18. Inverted baseline velocity model (m/s). FWI resolved fine model features and oriented them along the dip structure of the image in Figure 15 (the vertical axis depth is in meters and the horizontal axis inline is in meters).

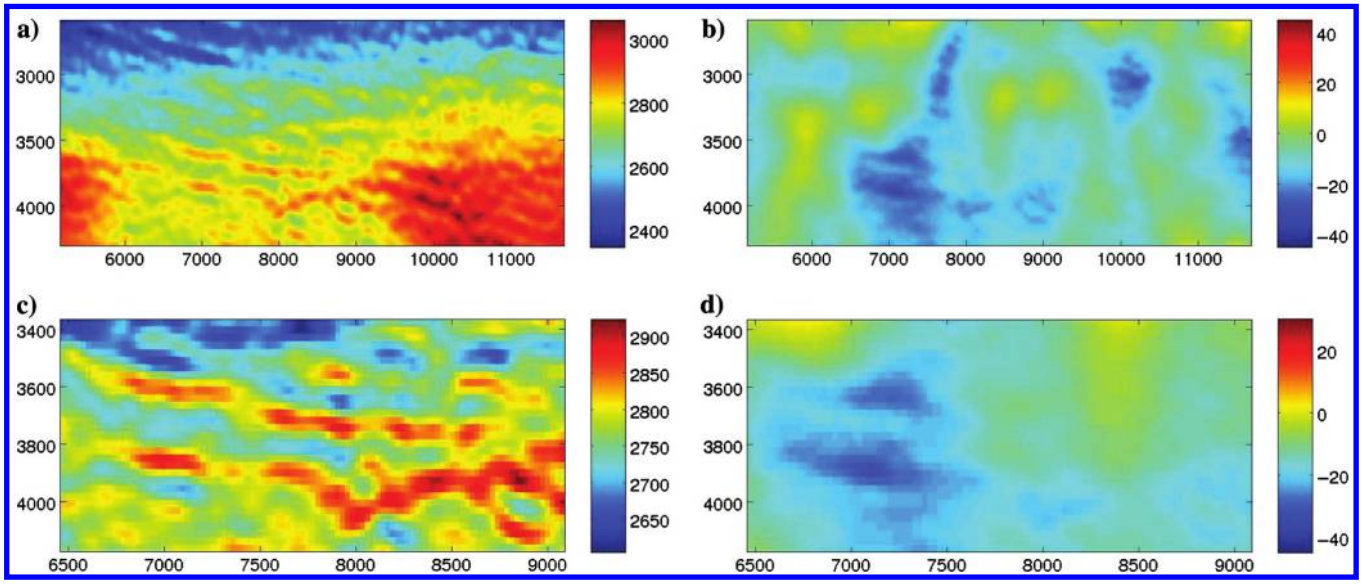

Figure 19. (a) Baseline target area and (b) estimated model difference for $\delta = 1000$. Close-up of (c) baseline target area and (d) estimated model difference for $\delta = 1000$.

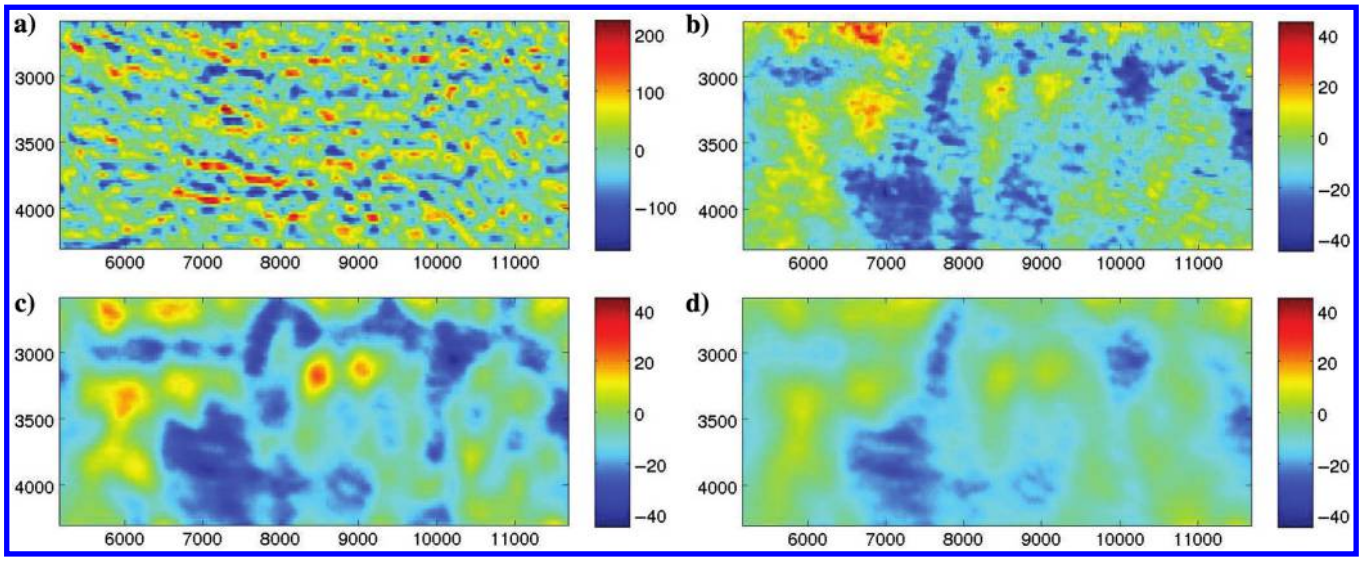

Figure 20. (a) Parallel-difference and joint-inversion results for (b) $\delta = 100$, (c) 500, and (d) 1000 in the target area. The parallel-difference result is not interpretable because of the presence of artifacts. Increasing the regularization parameter δ results in gradual removal of most model differences except the negative velocity change in the overburden, peaking around the Illinoisan sands and near the top of the stacked reservoirs (see Figure 19a–19d).

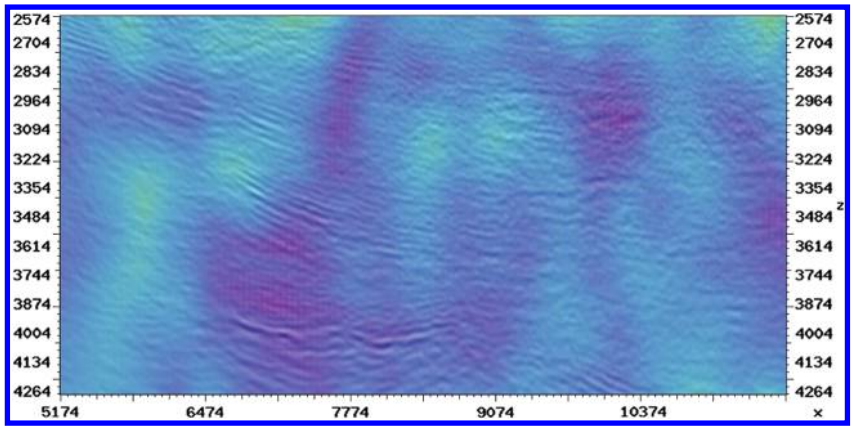

Figure 21. Inverted velocity difference interleaved with migrated image difference for baseline and monitor. The strongest image differences correspond to the top of Neb 1 reservoir and the Illinoisan sands above. Peaks of negative velocity change correlate with the overburden above the reservoir and the sands. The vertical axis depth is in meters, and the horizontal axis inline is in meters.

ACKNOWLEDGMENTS

The authors would like to thank S. A. Levin, J. P. Stefani, S. Ronen, and D. Bevc for several useful discussions; A. Cheng and two anonymous reviewers for their helpful suggestions; Stanford CEEES HPC and D. Michael for providing computing resources; and the affiliate members of Stanford Exploration Project for their support.

APPENDIX A

TIME-LAPSE SCATTERING APPROXIMATIONS

Acoustic scattering

Assuming a known background slowness $s(\mathbf{x}), \mathbf{x} \in \mathbb{R}^3$ (acoustic slowness is the reciprocal of acoustic velocity) and a slowness perturbation $\delta s(\mathbf{x})$, the total wavefield component $u(\mathbf{x})$ for frequency ω satisfies the Helmholtz equation

$$[\Delta + \omega^2(s(\mathbf{x}) + \delta s(\mathbf{x}))^2]u(\mathbf{x}) = -f(\mathbf{x}), \mathbf{x} \in D \subset \mathbb{R}^3, \quad \text{(A-1)}$$

where $f(\mathbf{x})$ is the seismic source component for frequency ω. The total wavefield is the sum of the incident and scattered wavefields

$$u(\mathbf{x}) = u_I(\mathbf{x}) + u_S(\mathbf{x}), \quad \text{(A-2)}$$

where the incident wavefield u_I satisfies the Helmholtz equation with the unperturbed slowness:

$$[\Delta + \omega^2 s^2(\mathbf{x})]u_I(\mathbf{x}) = -f(\mathbf{x}). \quad \text{(A-3)}$$

Note that for the well-posedness of problems for equations A-1 and A-3, we need to impose an additional condition on the solution, such as the Sommerfeld radiation condition for a homogeneous medium (Colton and Kress, 1998). Physically, such a condition requires that the total field be outgoing at infinity. We will assume that equations A-1 and A-3 are solved in a domain $D \subset \mathbf{R}^3$ and that absorbing boundary conditions (Engquist and Majda, 1977) are applied along the domain boundary, ensuring an outgoing propagation of the wavefields.

For time-lapse problems, we consider slowness perturbations $\delta s(\mathbf{x})$ with a support $\operatorname{supp} \delta s = \Gamma$, wholly contained in the interior of D, $\Gamma \subset \operatorname{int} D$. If $G(\mathbf{x}, \mathbf{y})$ is Green's function for the unperturbed Helmholtz equation A-3 in D and absorbing boundary conditions on ∂D, then equation A-1 is equivalent to the Lippmann-Schwinger integral equation

$$u_S(\mathbf{x},\mathbf{y}) = \omega^2 \int_D G(\mathbf{x},\mathbf{y})[(s(\mathbf{y}) + \delta s(\mathbf{y}))^2 - s^2(\mathbf{y})] \times [u_I(\mathbf{y}) + u_S(\mathbf{y})]d\mathbf{y}, \quad \text{(A-4)}$$

or, equivalently,

$$u_S(\mathbf{x}, \mathbf{y}) = \omega^2 \int_\Gamma G(\mathbf{x}, \mathbf{y})[(s(\mathbf{y}) + \delta s(\mathbf{y}))^2 - s^2(\mathbf{y})] \times [u_I(\mathbf{y}) + u_S(\mathbf{y})]d\mathbf{y}. \quad \text{(A-5)}$$

The expression in the first set of square brackets is a perturbation of the "slowness squared" denoted from now on as δs^2

$$\delta s^2(\mathbf{x}) = (s(\mathbf{x}) + \delta s(\mathbf{x}))^2 - s^2(\mathbf{x}) \approx 2\, s(\mathbf{x})\delta s(\mathbf{x}). \quad \text{(A-6)}$$

The incident wavefield $u_I(\mathbf{x})$ in equations A-4 and A-5 is assumed known.

Born series

Assuming that $\delta s^2 = O(\epsilon)$, where ϵ is the characteristic magnitude of a model perturbation, and formally representing the scattered wavefield as a Born scattering series

$$u_S(\mathbf{x}) = u_S^{(1)}(\mathbf{x}) + u_S^{(2)}(\mathbf{x}) + \cdots, \mathbf{x} = (x_1, x_2, x_3), \quad \text{(A-7)}$$

where

$$u_S^{(k)}(\mathbf{x}) = O(\epsilon^k), \quad k = 1, 2, \ldots, \quad \text{(A-8)}$$

we obtain

$$u_S^{(1)}(\mathbf{x}) = \omega^2 \int_\Gamma G(\mathbf{x}, \mathbf{y})\delta s^2(\mathbf{y})u_I(\mathbf{y})d\mathbf{y},$$
$$u_S^{(i+1)}(\mathbf{x}) = \omega^2 \int_\Gamma G(\mathbf{x}, \mathbf{y})\delta s^2(\mathbf{y})u_S^{(i)}(\mathbf{y})d\mathbf{y}. \quad \text{(A-9)}$$

Equations A-9 will help us to analyze the strengths of the Born series in equation A-7 in relating the diffracted wavefield $u_S(\mathbf{x})$ to $\delta s(\mathbf{x})$ for short-wavelength model perturbations, and its limitations for long-wavelength model perturbations. Assuming for demonstration purposes a homogeneous background $s(\mathbf{x}) = s_0$, and a constant finite δs, for a 3D medium, we have

$$G(\mathbf{x},\mathbf{y}) = \frac{\exp(i\omega s_0|\mathbf{x}-\mathbf{y}|)}{4\pi|\mathbf{x}-\mathbf{y}|}. \tag{A-10}$$

An incident plane wave propagating along axis $x = x_1$ is given by

$$u_I(\mathbf{x}) = \exp(i\omega s_0 x). \tag{A-11}$$

For a perturbation in a sufficiently small domain far from receiver locations

$$\forall\ \mathbf{y} \in \Gamma : |y_1| \ll x, \tag{A-12}$$

the denominator of expression A-10 is asymptotically a constant factor if $\mathbf{y} \in \Gamma$, and from equations A-6 and A-9, we obtain

$$\begin{aligned} u_S^{(1)}(x,0,0) &\approx \frac{\delta s^2 \cdot \omega^2}{4\pi|x-x^0|}\int_{\Gamma\cap\mathbb{R}^1}\exp(i\omega s_0(x-y_1)) \\ &\quad\times\exp(i\omega s_0 y_1)dy_1 \\ &= \frac{L\cdot\delta s^2\cdot\omega^2}{4\pi|x-x^0|}\exp(i\omega s_0 x), \\ &= \frac{L\cdot s_0\cdot\delta s\cdot\omega^2}{2\pi|x-x^0|}\exp(i\omega s_0 x), \end{aligned} \tag{A-13}$$

where

$$L = |\Gamma\cap\mathbb{R}^1(x)|, x^0 \in \Gamma\cap\mathbb{R}^1(x) \tag{A-14}$$

is length of the model perturbation along axis $\mathbb{R}^1(x)$, and x^0 is an arbitrary point within the support of δs. Note that inequality A-12 means that

$$|x^0| \ll |x|, \quad L \ll |x|. \tag{A-15}$$

The second inequality A-15 can be understood as a spikiness of the model perturbation because it is concentrated in a relatively small subset, compared with the characteristic model dimensions, such as the distance from a source of the incident wave (i.e., a subsurface reflector) to a surface receiver.

Equation A-13 means that the first-order Born scattering under our assumptions only accounts for the amplitude effects, but not the phase of the scattered wavefield. Indeed, phase changes (and time delays) accumulate in expression A-7 through the effect of the denominator in expression A-10, requiring progressively many terms to account for a phase delay or advance in the scattered (transmitted) wavefield. However, transmission through a constant perturbation δs of length L would cause a phase change proportional to $L\delta s$; therefore, any technique based on the truncated Born scattering would be suboptimal for relating long-wavelength, or blocky, velocity perturbations to measured scattered wavefields. This is a well-known limitation of diffraction tomography (Wu and Toksöz, 1987) that is inherited by any FWI using the standard time-domain L_2-misfit function (Fichtner, 2011). On the other hand, the Born series is a very good scattering approximation for short-wavelength large-amplitude perturbations as, again, demonstrated in equation A-13: Such perturbations have a first-order effect on the amplitude of the scattered wavefield.

Rytov series

The Rytov scattering series (Ishimaru, 1978; Rytov et al., 1989; Woodward, 1989) is based on an asymptotic phase expansion of the scattered wavefield and linearly relates phase changes with magnitudes of the slowness change to a first order, as does the initial approximation of FWI of phase misfits (Fichtner, 2011). To demonstrate that, let us again study the propagation of a planar incident wave A-11 through a perturbation δs. Under the Rytov scattering series, we represent the sum of the incident and scattered wavefields as

$$u_I(\mathbf{x}) + u_S(\mathbf{x}) = \exp[\phi^{(0)}(\mathbf{x}) + \phi^{(1)}(\mathbf{x}) + \phi^{(2)}(\mathbf{x}) + \cdots], \tag{A-16}$$

where

$$\phi^{(k)}(\mathbf{x}) = O(\epsilon^k), \quad k = 0, 1, 2, \ldots, \tag{A-17}$$

and ϵ is again the characteristic magnitude of the perturbation. Note that in equation A-16, phase terms $\phi^{(k)}(\mathbf{x})$ may have nonzero real and imaginary parts, with the real parts determining solution amplitude. Substituting equations A-16 and A-17 into equation A-1 and assuming that

$$u_I(\mathbf{x}) = \exp[\phi^{(0)}(\mathbf{x})], \tag{A-18}$$

after grouping together the terms of the same order of magnitude, we obtain

$$\Delta\phi^{(0)}(\mathbf{x}) + |\nabla\phi^{(0)}(\mathbf{x})|^2 + \omega^2 s^2(\mathbf{x}) = -f(\mathbf{x}), \tag{A-19}$$

and

$$\begin{aligned} &\Delta\phi^{(1)}(\mathbf{x}) + 2\langle\nabla\phi^{(0)}(\mathbf{x}), \phi^{(1)}(\mathbf{x})\rangle \\ &\quad + |\nabla\phi^{(1)}(\mathbf{x})|^2 + \omega^2\delta s^2(\mathbf{x}) = 0, \end{aligned} \tag{A-20}$$

where only the first two terms of the Rytov series A-16 are used. Assuming, for simplicity, a constant background s_0 and a constant finite perturbation δs, the phase change for a transmitted plane wave traveling through a perturbation δs of characteristic dimension L is approximately proportional to $L\delta s^2/(2s_0) \approx L\delta s$. Indeed, the plane-wave solution A-11 satisfies equation A-19 outside of supp f. Assuming a heterogeneity along the x-axis only, hence

$$\phi^{(1)}(\mathbf{x}) = \phi^{(1)}(x), \tag{A-21}$$

we obtain

$$\begin{aligned} &\frac{d^2}{dx^2}\phi^{(1)}(x) + \left[\frac{d}{dx}\phi^{(1)}(x)\right]^2 + 2i\omega s_0\frac{d}{dx}\phi^{(1)}(x) \\ &\quad + \omega^2\delta s^2(x) = 0. \end{aligned} \tag{A-22}$$

If slowness perturbations are small in magnitude

$$|\delta s| \ll 1 \Rightarrow \left|\frac{\delta s^2}{s_0}\right| \ll 1, \tag{A-23}$$

we can drop the second term in equation A-22 because it is of order $O(\epsilon^2)$ to obtain

$$\frac{d^2}{dx^2}\phi^{(1)}(x) + 2i\omega s_0 \frac{d}{dx}\phi^{(1)}(x) + \omega^2 \delta s^2(x) = 0. \quad \text{(A-24)}$$

Furthermore, assuming that the perturbed phase is slowly changing in space, we can drop the first term to obtain the following equation that governs a strictly imaginary phase (thus producing a phase-only Rytov approximation):

$$\begin{aligned}\phi^{(1)}(x) &\approx i\omega \int_{-\infty}^{x} \frac{\delta s^2(\eta)}{2s_0} d\eta = i\omega \int_{\Gamma} \frac{\delta s^2(\eta)}{2s_0} d\eta, \\ &\approx i\omega \int_{\Gamma} \frac{2s_0 \delta s(\eta)}{2s_0} d\eta = i\omega \int_{\Gamma} \delta s(\eta) d\eta. \end{aligned} \quad \text{(A-25)}$$

Note that the discarded term in equation A-24 contributes to the real phase component, and thus accounts for amplitude effects. Let us now analyze the order of magnitude of amplitude effects that can be estimated by solving the full equation A-24. Solving the linear equation with constant coefficients, we obtain

$$\frac{d}{dx}\phi^{(1)}(x) = -\omega^2 \int_{-\infty}^{x} e^{-2i\omega s_0(x-\eta)} \delta s^2(\eta) d\eta, \quad \text{(A-26)}$$

and after integration by parts,

$$\begin{aligned}\frac{d}{dx}\phi^{(1)}(x) &= -\frac{\omega^2}{2i\omega s_0} \int_{-\infty}^{x} \delta s^2(\eta) de^{-2i\omega s_0(x-\eta)} \\ &= \frac{i\omega}{2s_0}\delta s^2(x) - \frac{i\omega}{2s_0}\int_{-\infty}^{x} e^{-2i\omega s_0(x-\eta)}[\delta s^2(\eta)]' d\eta \\ &= \frac{i\omega}{2s_0}\delta s^2(x) - \frac{1}{4s_0^2}[\delta s^2(x)]' \\ &\quad + \tfrac{1}{4s_0^2}\textstyle\int_{-\infty}^{x} e^{-2i\omega s_0(x-\eta)}[\delta s^2(\eta)]'' d\eta \\ &= \tfrac{i\omega}{2s_0}\delta s^2(x) + \textstyle\sum_{k=1}^{+\infty} \frac{i\omega}{2s_0(-2i\omega s_0)^k}[\delta s^2(x)]^{(k)}, \end{aligned} \quad \text{(A-27)}$$

where we assume that the derivatives of squared slowness perturbation ultimately become negligible, $[\delta s^2]^{(k)} \sim 0$. The first term in the right side of equation A-27 yields the first-order phase shift of equation A-25 after integration. The odd terms of the series in equation A-27 are phases with nonzero real parts and contribute to the amplitude of the scattered wave. Note that significant oscillations of model perturbation δs^2 may result in large spikes of the slowness derivative and thus affect the scattered amplitude. On the other hand, oscillatory model perturbations with zero average have negligible effect on the phase and, by extension, traveltime of the scattered wave (see equation A-25).

It should be noted that while the requirement of perturbation spikiness in inequality A-15 is critical for the accuracy of the Born approximation, the requirement of blockiness and small variation of the slowness perturbation is not necessary for the accuracy of the Rytov approximation with a full complex phase. Indeed, solution of the second-order ordinary differential equation A-24 shown in equation A-27 accounts for the amplitude and phase effects of perturbation oscillations. However, in the absence of significant perturbation oscillations, there is a simple linear relationship between the slowness perturbation and phase change (or time shift) of expression A-25 that is equivalent to the linearized traveltime tomography approximation.

REFERENCES

Al-Najjar, N., I. Brevik, L. Kvamme, D. Psaila, and P. Doyen, 1999, Statfjord field time lapse seismic interpretation using a 4D earth model: 69th Annual International Meeting, SEG, Expanded Abstracts, 1620–1623.

Asnaashari, A., R. Brossier, S. Garambois, F. Audebert, P. Thore, and J. Virieux, 2012, Time-lapse imaging using regularized FWI: A robustness study: 82nd Annual International Meeting, SEG, Expanded Abstracts, doi: 10.1190/segam2012-0699.1.

Aster, R., B. Borchers, and C. H. Thurber, 2011, Parameter estimation and inverse problems: Academic Press.

Auer, L., A. M. Nuber, S. A. Greenhalgh, H. Maurer, and S. Marelli, 2013, A critical appraisal of asymptotic 3D-to-2D data transformation in full-waveform seismic crosshole tomography: Geophysics, **78**, no. 6, R235–R247, doi: 10.1190/geo2012-0382.1.

Ayeni, G., 2011, Time-lapse seismic imaging by linearized joint inversion: Ph.D. thesis, Stanford University.

Ayeni, G., and B. Biondi, 2012, Time-lapse seismic imaging by linearized joint inversion: A Valhall Field case study: 82nd Annual International Meeting, SEG, Expanded Abstracts, doi: 10.1190/segam2012-0903.1.

Barkved, O. I., and T. Kristiansen, 2005, Seismic time-lapse effects and stress changes: Examples from a compacting reservoir: The Leading Edge, **24**, 1244–1248, doi: 10.1190/1.2149636.

Boyd, S., N. Parikh, E. Chu, B. Peleato, and J. Eckstein, 2011, Distributed optimization and statistical learning via the alternating direction method of multipliers: Foundations and Trends in Machine Learning, **3**, 1–122, doi: 10.1561/2200000016.

Buland, A., and Y. E. Ouair, 2006, Bayesian time-lapse inversion: Geophysics, **71**, no. 3, R43–R48, doi: 10.1190/1.2196874.

Colton, D., and R. Kress, 1998, Inverse acoustic and electromagnetic scattering theory: Applied mathematical sciences, 2nd ed.: Springer.

Engquist, B., and A. Majda, 1977, Absorbing boundary conditions for the numerical simulation of waves: Mathematics of Computation, **31**, 629–629, doi: 10.1090/S0025-5718-1977-0436612-4.

Fichtner, A., 2011, Full seismic modeling and inversion: Springer.

Gawith, D. E., and P. Gutteridge, 1996, Seismic validation of reservoir simulation using a shared earth model: Petroleum Geoscience, **2**, 97–103, doi: 10.1144/petgeo.2.2.97.

Goldstein, T., and S. Osher, 2009, The split Bregman method for L1-regularized problems: SIAM Journal on Imaging Sciences, **2**, 323–343, doi: 10.1137/080725891.

Gouveia, W. P., D. H. Johnston, A. Solberg, and M. Lauritzen, 2004, Jotun 4D: Characterization of fluid contact movement from time-lapse seismic and production logging tool data: The Leading Edge, **23**, 1187–1194, doi: 10.1190/1.1825941.

Grana, D., and T. Mukerji, 2014, Bayesian inversion of time-lapse seismic data for the estimation of statis reservoir properties and dynamic property changes: Geophysical Prospecting, **63**, 637–655, doi: 10.1111/1365-2478.12203.

Hatchell, P., and S. Bourne, 2005, Measuring reservoir compaction using time-lapse timeshifts: 75th Annual International Meeting, SEG, Expanded Abstracts, 2500–2503.

Herwanger, J. V., 2008, R we there yet?: 70th Annual International Conference and Exhibition, EAGE, Extended Abstracts, I029.

Hodgson, N., C. Macbeth, L. Duranti, J. Rickett, and K. Nihei, 2007, Inverting for reservoir pressure change using time-lapse time strain: Application to Genesis Field, Gulf of Mexico: The Leading Edge, **26**, 649–652, doi: 10.1190/1.2737104.

Holt, R. M., O.-M. Nes, and E. Fjaer, 2005, In-situ stress dependence of wave velocities in reservoir and overburden rocks: The Leading Edge, **24**, 1268–1274, doi: 10.1190/1.2149650.

Hudson, T., B. Regel, J. Bretches, P. Condon, J. Rickett, B. Cerney, and P. Inderwiesen, 2005, Genesis Field, Gulf of Mexico, 4D project status and preliminary lookback: 75th Annual International Meeting, SEG, Expanded Abstracts, 2436–2439.

Ishimaru, A., 1978, Wave propagation and scattering in random media: Academic Press.

Johnston, D., 2013, Practical applications of time-lapse seismic data: SEG.

Landrø, M., 2001, Discrimination between pressure and fluid saturation changes from time-lapse seismic data: Geophysics, **66**, 836–844, doi: 10.1190/1.1444973.

Lumley, D. E., 1995, Seismic time-lapse monitoring of subsurface fluid flow: Ph.D. thesis, Stanford University.

Lumley, D. E., A. Nur, S. Strandenes, J. Dvorkin, and J. Packwood, 1994, Seismic monitoring of oil production: A feasibility study: 64th Annual International Meeting, SEG, Expanded Abstracts, 319–322.
Ma, Y., M. Maharramov, R. Clapp, and B. Biondi, 2015, Illumination compensation by L1 regularization and steering filters: Stanford Exploration Project Report 158, 279–290.
Magesan, M., S. Depagne, K. Nixon, B. Regel, J. Opich, G. Rogers, and T. Hudson, 2005, Seismic processing for time-lapse study: Genesis Field, Gulf of Mexico: The Leading Edge, **24**, 364–373, doi: 10.1190/1.1901384.
Maharramov, M., and U. Albertin, 2007, Localized image-difference wave-equation tomography: 77th Annual International Meeting, SEG, Expanded Abstracts, 3009–3013.
Maharramov, M., and B. Biondi, 2014a, Joint full-waveform inversion of time-lapse seismic data sets: 84th Annual International Meeting, SEG, Expanded Abstracts, 954–959, doi: 10.1190/segam2014-0962.1.
Maharramov, M., and B. Biondi, 2014b, Multi-model full-waveform inversion: Stanford Exploration Project Report 155, 187–192.
Maharramov, M., B. Biondi, and M. Meadows, 2015a, Simultaneous TV-regularized time-lapse FWI with application to field data: 85th Annual International Meeting, SEG, Expanded Abstracts, 1236–1241.
Maharramov, M., B. Biondi, and S. Ronen, 2015b, Robust simultaneous time-lapse full-waveform inversion with total-variation regularization of model difference: 77th Annual International Conference and Exhibition, EAGE, Extended Abstracts, We P3 09.
Meyer, Y., 2001, Oscillating patterns in image processing and nonlinear evolution equations. The Fifteenth Dean Jacqueline B. Lewis Memorial Lectures: American Mathematical Society.
Nocedal, J., and S. J. Wright, 2006, Numerical optimization: Springer.
Nur, A. M., 1982, Seismic imaging in enhanced recovery: SPE Enhanced Oil Recovery Symposium, SPE-10680–MS.
Raknes, E., W. Weibull, and B. Arntsen, 2013, Time-lapse full waveform inversion: Synthetic and real data examples: 83rd Annual International Meeting, SEG, Expanded Abstracts, 944–948.
Rickett, J., L. Duranti, T. Hudson, and N. Hodgson, 2006, Compaction and 4D time strain at the Genesis Field: 76th Annual International Meeting, SEG, Expanded Abstracts, 3215–3219.
Rickett, J., L. Duranti, T. Hudson, B. Regel, and N. Hodgson, 2007, 4D time strain and the seismic signature of geomechanical compaction at Genesis: The Leading Edge, **26**, 644–647, doi: 10.1190/1.2737103.
Routh, P., G. Palacharla, I. Chikichev, and S. Lazaratos, 2012, Full wavefield inversion of time-lapse data for improved imaging and reservoir characterization: 82nd Annual International Meeting, SEG, Expanded Abstracts, doi: 10.1190/segam2012-1043.1.
Rudin, L. I., S. Osher, and E. Fatemi, 1992, Nonlinear total variation based noise removal algorithms: Physica D: Nonlinear Phenomena, **60**, 259–268, doi: 10.1016/0167-2789(92)90242-F.
Rytov, S. M., Y. A. Kravtsov, and V. I. Tatarski, 1989, Principles of statistical radiophysics 4: Wave propagation through random media: Springer.
Sirgue, L., O. I. Barkved, J. Dellinger, J. Etgen, U. Albertin, and J. Kommedndal, 2010a, Full waveform inversion: The next leap forward in imaging at Valhall: First Break, **28**, 65–70, doi: 10.3997/1365-2397.2010012.
Sirgue, L., J. T. Etgen, U. Albertin, and S. Brandsberg-Dahl, 2010b, System and method for 3D frequency domain waveform inversion based on 3D time-domain forward modeling: U.S. Patent 7,725,266.
Sirgue, L., J. T. Etgen, and U. Albertin, 2008, 3D frequency domain waveform inversion using time domain finite difference methods: 70th Annual International Conference and Exhibition, EAGE, Extended Abstracts, F022.
Sirgue, L., and R. Pratt, 2004, Efficient waveform inversion and imaging: A strategy for selecting temporal frequencies: Geophysics, **69**, 231–248, doi: 10.1190/1.1649391.
Slaney, M., A. C. Kak, and L. E. Larsen, 1984, Limitations of imaging with first-order diffraction tomography: IEEE Transactions on Microwave Theory and Techniques, **32**, 860–874, doi: 10.1109/TMTT.1984.1132783.
Tadmor, E., S. Nezzar, and L. Vese, 2004, A multiscale image representation using hierarchical (BV, L^2) decompositions: Multiscale Modeling and Simulation, **2**, 554–579, doi: 10.1137/030600448.
Tikhonov, A. N., and V. Y. Arsenin, 1977, Solution of ill-posed problems: Winston & Sons.
Trani, M., R. Arts, O. Leeuwenburgh, and J. Brouwer, 2011, Estimation of changes in saturation and pressure from 4D seismic AVO and time-shift analysis: Geophysics, **76**, no. 2, C1–C17, doi: 10.1190/1.3549756.
Watts, G. F. T., D. Jizba, D. E. Gawith, and P. Gutteridge, 1996, Reservoir monitoring of the Magnus field through 4D-seismic analysis: Petroleum Geoscience, **2**, 361–372, doi: 10.1144/petgeo.2.4.361.
Woodward, M. J., 1989, Wave equation tomography: Ph.D. thesis, Stanford University.
Wu, R.-S., and M. N. Toksöz, 1987, Diffraction tomography and multisource holography applied to seismic imaging: Geophysics, **52**, 11–25, doi: 10.1190/1.1442237.
Yang, D., A. E. Malcolm, and M. C. Fehler, 2014, Time-lapse full waveform inversion and uncertainty analysis with different survey geometries: 76th Annual International Conference and Exhibition, EAGE, Extended Abstracts, We ELI1 10.
Yuh, S. H., S. Yoon, J. Richard, L. Gibson, and A. DattaGupta, 2000, Effects of pressure and fluid saturation changes on time-lapse AVO response: 70th Annual International Meeting, SEG, Expanded Abstracts, 1481–1484.
Zheng, Y., P. Barton, and S. Singh, 2011, Strategies for elastic full waveform inversion of time-lapse ocean bottom cable (OBC) seismic data: 81st Annual International Meeting, SEG, Expanded Abstracts, 4195–4200.
Zoback, M., 2010, Reservoir geomechanics: Cambridge University Press.